# Scaling Analysis for the Interaction between a Buoyant Coastal Current and the Continental Shelf: Experiments and Observations

GREG AVICOLA AND PABLO HUQ

*College of Marine Studies, University of Delaware, Newark, Delaware*

(Manuscript received 10 October 2001, in final form 22 May 2002)

ABSTRACT

This paper addresses how the geometrical parameters (ambient ocean depth, $H$; bottom slope, $\alpha$) of coastal bathymetry affect the evolution of buoyant coastal currents flowing over a sloping continental shelf. Scaling arguments are presented that show the coastal current dynamics can be classified by a two-variable nondimensional parameter space: the ambient depth parameter, $h/H$, and the bottom slope parameter, $R/y_b$. The ratio $h/H$ is the fraction of the available depth occupied by the buoyant layer; the bottom slope parameter is the ratio of two horizontal length scales, the internal Rossby radius $R$ to the bottom-trapped width $y_b$. The scale depth $h$ is derived from geostrophic dynamics and is representative of the depth of the buoyant layer of the coastal current. The resulting parameter space is delineated by surface-advected currents that do not depend upon the bottom slope parameter and bottom-trapped currents that do. For bottom-trapped coastal currents, the across-shore width and downstream velocities are dependent upon the magnitude of the bottom slope parameter, $R/y_b$. The bottom slope parameter is also a ratio of the buoyant layer isopycnal slope to the shelf slope. Experiments are conducted in the laboratory in order to test the scaling. Measurements of coastal current width and nose velocities are taken, together with mean density cross sections, for a number of coastal currents. Experimental observations and oceanic datasets are examined in terms of the proposed scaling arguments; it is shown that these experimental measurements and oceanic observations are in accord.

## 1. Introduction

Freshwater river outflow is an important component in the dynamics of coastal waters. Such outflows enter the coastal ocean through a river, estuary, or strait to often form a coastal current. The physics of coastal currents, and its impact on the biology of coastal waters, should be better understood. Our limited knowledge of the dynamics of coastal currents is a consequence of the cost of ship deployment and large mooring arrays, which limits the spatial and temporal resolution of observational studies. The objective of this paper is to examine the characteristics and evolution of idealized coastal currents in laboratory experiments and to compare with simple theory. The classification of the dynamics of coastal currents is based on two coastal geometric parameters: ambient water depth $H$ and slope $\alpha$ of the bottom boundary, and three source parameters: flow rate $Q$, reduced gravity $g'$, and the local Coriolis parameter $f$. The laboratory results and a proposed scaling will be compared with available oceanic observations.

Buoyant outflows occur commonly and have been studied in various localities throughout the world. Observations of the Connecticut River include studies by Garvine (1974, 1977) and Garvine and Monk (1974). The Columbia River plume was studied by Stefansson and Richards (1963), Park (1966), and Hickey et al. (1998). Boicourt (1973) and Rennie et al. (1999) observed the Chesapeake Bay outflow, noting that it formed a coastal current that persisted as far as Cape Hatteras. The Delaware coastal current has been studied in detail. Münchow and Garvine (1993a,b) and Sanders and Garvine (1996) investigated the propagation of buoyant coastal waters outside of the estuary and downstream along the coast. Blanton and Atkinson (1983) observed coastal current formation from river outflows in the South Atlantic Bight, and Bracalari et al. (1989) examined coastal currents in Sicily formed from numerous river outflows. Buoyant outflows can be formed from other processes besides river discharges. Outflow from oceanic straits in which there are significant density differences arising from either temperature or salinity can also form coastal currents. Ichiye (1984, 1991) and Sugimoto (1990) described buoyant water flowing through the Tsushima, Soya, and Tsugaru Straits that formed coastal currents.

Previous laboratory studies have established some aspects of the evolution of coastal currents. Stern et al. (1982) examined a buoyant coastal current using a rotating rectangular tank in which buoyant fluid was released from a lock-exchange (or dam-break) setup. Their

*Corresponding author address:* Dr. Pablo Huq, College of Marine Studies, Robinson Hall, University of Delaware, Newark, DE 19716. E-mail: huq@udel.edu

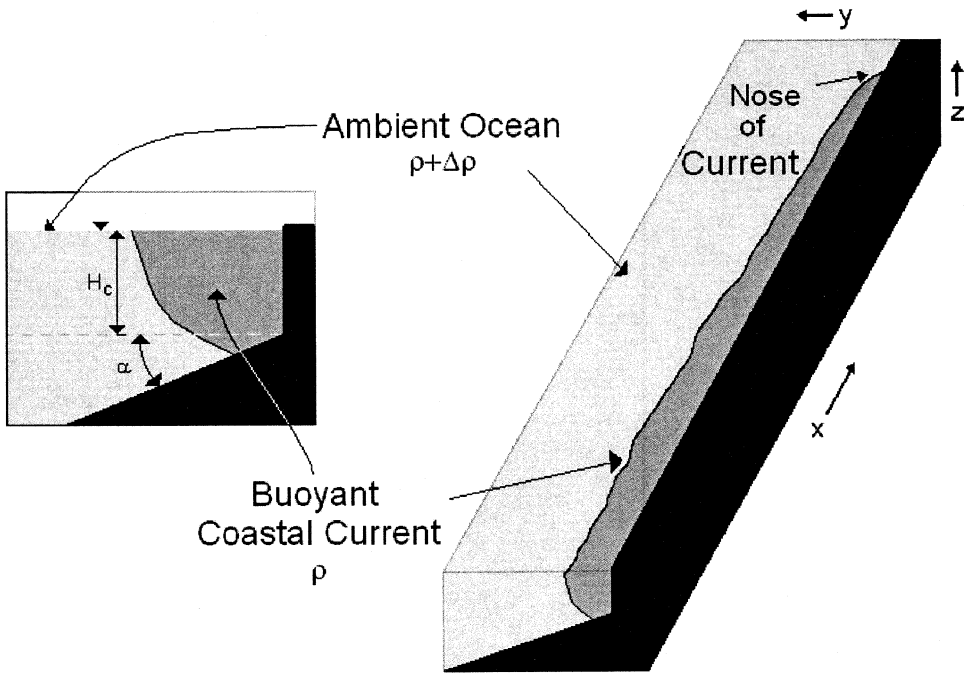


FIG. 1. Schematic portraying a representative coastal topography. The simplified geometry consists of a coastline that is uniform in the along-shelf direction. The across shelf variation is described by a coastal wall depth $H_c$ and a bottom slope $\alpha$. The coastal wall depth $H_c$ may be zero. The coordinate system used is as follows: positive $x$ is along shelf with the coast on the right (the direction of Kelvin wave propagation in the Northern Hemisphere), positive $y$ points across shelf from the coastline, and positive $z$ is vertically upward from the ocean surface.

research focus was on the geometry and propagation of the leading edge (or nose) of the coastal current. Whitehead and Chapman (1986) utilized a sloping bottom configuration in a circular tank for their experiments: they observed that the sloping bottom had a dynamically significant effect on the evolution of the coastal current. The stability of coastal currents was examined by D'Hieres et al. (1991): the wavelengths of the instabilities were found to decrease with increasing values of the ratio of the Rossby radius to the coastal current source width.

Attempts to classify the dynamics of coastal currents have been undertaken previously. Chao (1988) suggested a classification scheme based upon an internal Froude number and a dissipation parameter. He divided coastal current evolution into four dynamical groups: subcritical, supercritical, diffusive-subcritical, and diffusive-supercritical. Garvine (1995) proposed a classification scheme based upon the coastal current Kelvin number, delineating between ''large scale'' buoyant plumes ($K > 1$) that form coastal currents and ''small scale'' plumes ($K < 1$) that develop with minimal influence from planetary rotation. Yankovsky and Chapman (1997) suggested a classification scheme, which segregates coastal currents into bottom-trapped, surface-advected, and intermediate currents, based on a ratio of the ambient water depth to the depth of the buoyant layer. Lentz and Helfrich (2002) investigate the effect of coastal current–bathymetry interaction through a ratio of velocities, the ''vertical wall limit'' to the ''slope-control limit,'' which scales the problem in a similar manner to that presented here.

This paper will attempt to address how the coastal geometrical parameters (ambient ocean depth $H$ and bottom slope $\alpha$) affect the development of buoyant coastal currents. Scaling arguments will be presented that show the coastal current dynamics are classifiable by a two-variable nondimensional parameter space comprising an ambient depth parameter and a bottom slope parameter. The robustness of the classification will be examined using laboratory simulations of coastal currents and compared with available oceanic data. The configuration of the idealized problem is shown in Fig. 1. The scale of horizontal variations in the coastal bathymetry should be much larger than the internal Rossby radius for this scaling to hold. The geometry of the across-shore depth profile can be defined by a coastal wall depth $H_c$ and a bottom slope $\alpha$. The buoyant current is produced by placing a constant outflow source parallel to the coastal wall. (Thus the angle between the coastal wall and the outflow source is 0°.) Experiments were conducted in this manner to remove any effects due to nonzero angles from the configuration. Previous laboratory and numerical studies (Pichevin and Nof 1997; Fong 1998; Nof and Pichevin 2001) have shown that for large an-

gles, the formation and evolution of a bulge region affects downstream coastal current dynamics.

Section 2 introduces the proposed scaling and nondimensional parameter space. Schematics are presented to illustrate the interaction of the coastal current with the sloping bottom. Section 3 describes the setup of the laboratory experiments. Section 4 presents the data collected; flows were segregated into surface-advected and bottom-trapped coastal currents. Finally, section 5 discusses oceanic observations of coastal currents classified in terms of the proposed nondimensional parameter space.

## 2. Coastal current–shelf interaction scaling

The interplay between the buoyant outflow and variations of depth and slope of the ambient shelf geometry is considered. A natural starting point for this exercise is the examination of the dynamics of coastal currents unaffected by the bottom (i.e., deep ambient coastal waters). For a coastal current occurring in a deep ocean against a vertical sidewall, volume conservation between the source outflow and the flow in the current can be written as

$$Q = \int\int_A u \, \partial z \, \partial y = \int_0^L u\zeta \, \partial y, \tag{1}$$

where $Q$ is the source flow rate; $u$ is the downstream velocity; $\zeta$ is the layer depth, which varies with offshore distance $y$; and $L$ is the offshore extent of the coastal current. The primary assumption is that the frontal dynamics are that of a Margules front. Thermal wind balance for a Margules front is written as

$$u = \frac{g'}{f}\frac{\partial \zeta}{\partial y}. \tag{2}$$

Solving this simple system results in the coastal-current scale variables used in this paper:

$$h = \zeta_0 = \sqrt{\frac{2Qf}{g'}} \tag{3}$$

$$R = \frac{\sqrt{g'h}}{f} = \frac{(2Qg')^{1/4}}{(f)^{3/4}} \tag{4}$$

$$c = \sqrt{g'h} = (2Qg'f)^{1/4}. \tag{5}$$

These three scales are the coastal current scales: $h$ is the scale depth, $R$ is the baroclinic Rossby deformation radius, and $c$ is the internal wave phase speed. Equations (3)–(5) are used to nondimensionalize the coastal current depth, width, and velocity, respectively. The scales require knowledge of only source conditions, $Q$ (outflow rate), $g'$ (reduced gravity calculated from the value of the maximum density anomaly at the source), and $f$ (local Coriolis parameter).

There are a number of assumptions implicit in this scaling; primarily it is assumed that the front is in geostrophic balance to first order. Also, mixing within the current must be relatively small. This is evident in Eq. (1), which requires that the volume flux at the source is (approximately) equal to the volume flux in the (downstream) frontal structure. Note that in previous experiments and simulations (e.g., Pichevin and Nof 1997; Nof and Pichevin 2001) with a 90° angle between the buoyant source and the vertical wall, the volume flux does not entirely flow into the coastal current; rather, some fraction is trapped in a bulge recirculation region. For this study, however, the volume flux from the source is released parallel to the coastline, thereby removing this complication of bulge dynamics from the problem.

Figure 2 depicts typically observed situations of coastal currents with arbitrary bottom topography. Figure 2a is a schematic of a surface-advected current (e.g., Yankovsky and Chapman 1997) in which only a small portion of the coastal current is in contact with the bottom. In contrast, Fig. 2b depicts a bottom-trapped current in which most of the coastal current is in contact with the bottom. In order to address possible variations of bottom topography a scaling is proposed that includes a single bottom slope $\alpha$ and a coastal wall depth $H_c$. The ambient ocean depth $H$ is defined as the depth of the fluid column at one Rossby radius $R$ offshore ($H$ = depth at $1.0R = H_c + \alpha R$). Previous observations demonstrate that a coastal current is typically a few Rossby radii in width (Garvine 1995). This scheme is used to estimate an effective bottom depth $H$ based on the scale of the plume, in a simple and robust manner.

A bottom topography without a vertical wall such as that drawn in Figs. 2a and 2b can be approximated by a single bottom slope $\alpha$. In this situation, the equation describing the ambient ocean depth $H$ becomes the simple expression $H = \alpha R$. Many locations in the ocean can be approximated by this case. However, this is not the only realistic configuration. Figure 2c depicts a coastal topography that can be approximated with a two-slope configuration in which the nearshore slope, $\alpha_1$, is much larger than the offshore slope, $\alpha_2$. This approximation is shown in Fig. 2d. In this situation, the ambient ocean depth $H$ is equal to $H = \alpha_1 y_1 + \alpha_2(R - y_1)$. Because $\alpha_1$ is much larger than $\alpha_2$, the first slope can be approximated as a vertical wall of depth $H_c$. In this situation, the ambient ocean depth $H$ can be approximated as $H = H_c + \alpha_2 R$. Oceanic coastal currents have been observed in regions with such compound slopes, such as the Rhine (Charnock et al. 1994) and the Delaware (Munchow and Garvine 1993b). Additionally, this situation is common in laboratory (e.g., Whitehead and Chapman 1986) and numerical simulations (e.g., Yankovsky and Chapman 1997) of coastal currents, and is the case used in this study as well. Thus, the scale, $H = H_c + \alpha R$, is proposed as a useful measure in estimating the ambient depth of the local ocean. As seen in Table 1, this parameterization produces reasonable values for $H$ for a wide variety of locations with varying

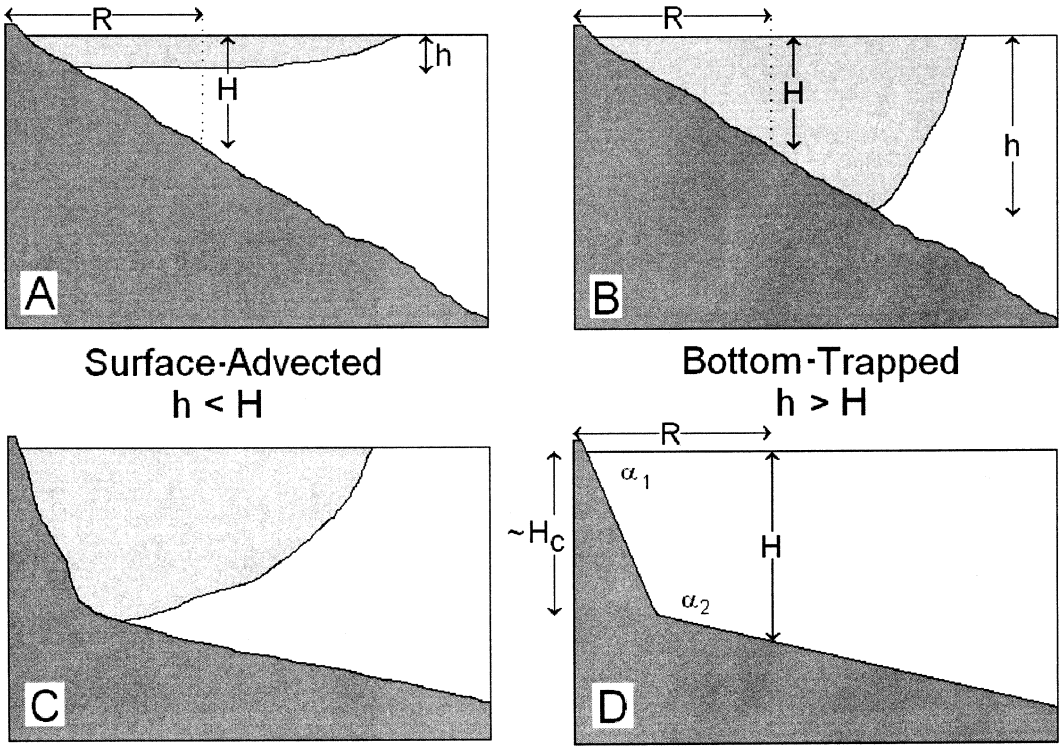


FIG. 2. Schematic that portrays surface-advected and bottom-trapped coastal currents over a variety of topographies. As described in section 2, the ambient ocean depth $H$ is defined as the ambient depth one Rossby radius offshore, $R$. In this manner, the effect of coastal walls or initial steep slopes can be accounted for in the parameter space without an explicit functional form for the specific coastal bathymetry affecting a particular current. The scale depth of the buoyant layer is designated by $h$. Idealized schematics in which a bottom that can be characterized by a single slope ($\alpha$) can produce (a) surface-advected and (b) bottom-trapped coastal currents. (c) A situation in which a concave coastal bathymetry can be represented by two bottom slope values. (d) This can be further simplified as a coastal wall and a bottom slope.

coastal bathymetries. To summarize, the nondimensional ambient depth parameter $h/H$ is

$$\frac{h}{H} = \frac{h}{\text{depth @ } 1R} = \frac{h}{H_c + \alpha R}. \tag{6}$$

When the value of this parameter is small ($h/H < 1$), the coastal current is surface-advected; that is, the coastal current is not in contact with the bottom over the majority of its extent. Conversely, when this parameter is large ($h/H > 1$) the coastal current is bottom-trapped and, thus, feels the influence of the bottom.

The theory of Chapman and Lentz (1994) is utilized to scale the interaction of the buoyant coastal current with the bottom. They hypothesize that the offshore buoyancy flux of a buoyant coastal current interacting with the bottom occurs in a thin bottom Ekman layer. The Ekman layer transports buoyant fluid offshore until it reaches its trapped distance, which occurs at the point offshore at which the geostrophic layer above obtains a downshelf velocity of zero at the Ekman layer. This trapped distance is an important scale for the bottom-trapped coastal current. Chapman and Lentz begin this analysis from a force balance in the bottom Ekman layer of thickness $\delta$:

$$-f \int_{-H}^{-H+\delta} v\partial z = -\frac{\delta}{\rho_0}\frac{\partial P}{\partial x} - ru_b. \tag{7}$$

Note that in Eq. (7) the layer above the bottom Ekman layer is assumed to be in geostrophic balance to first order. This allows use of the thermal wind to describe the velocities of the upper layer, as shown in Eq. (8):

$$u_b = u_{\max} - h\frac{g}{f\rho_0}\frac{\partial \rho}{\partial y}. \tag{8}$$

Equations 7 and 8 can be combined to solve for the point at which the cross-shore velocity goes to zero as Eq. (8) relates the velocity in the bottom Ekman layer to the velocity at the surface. The offshore extent of this bottom-trapped layer is given by $y_b$:

$$y_b \sim \frac{f\rho}{\alpha g}\frac{u_{\max}}{\partial\rho/\partial y}\left[1 + \frac{\delta(\partial P/\partial x)}{\rho_0 r u_{\max}}\right]. \tag{9}$$

Equation (9) can be approximated as

$$y_b \sim \frac{f\rho}{\alpha g}\frac{u_{\max}}{\partial\rho/\partial y} \tag{10}$$

as the value of the term inside the brackets of Eq. (9)

TABLE 1. Parameters used in describing oceanic coastal currents. The value for $Q$ and $g'$ are taken at the source of the river or estuary, wherever applicable. The values are derived from references that give $g'$ at the mouth of the estuary and the flow rate of the river; $Q$ is therefore increased to include the mixing prior to exiting onto the shelf. Values for $H_c$ and $\alpha$ are found from the local bathymetry of the coast. These are taken from the referenced papers or charts of the region.

| Outflow | $Q$ ($m^3$ $s^{-1}$) | $f$ ($s^{-1}$) | $g'$ ($m$ $s^{-2}$) | $H_c$ (m) | $\alpha$ | $h$ (m) | $R$ (m) | $H$ (m) | $h/H$ | $R/y_b$ | References |
|---|---|---|---|---|---|---|---|---|---|---|---|
| Delaware | $1.6 \times 10^4$ | $9.09 \times 10^{-5}$ | 0.039 | 10 | 0.0007 | 8.68 | $6.37 \times 10^3$ | 14 | 0.600 | 0.514 | Sanders and Garvine (1996)<br>Munchow and Garvine (1993b)<br>Munchow and Garvine (1993a) |
| Rio De La Plata | $2.5 \times 10^4$ | $7.27 \times 10^{-5}$ | 0.245 | 0 | 0.0007 | 3.85 | $1.34 \times 10^4$ | 9 | 0.412 | 2.428 | A. Munchow (2001; personal communication) |
| Rhine | $1.9 \times 10^4$ | $1.15 \times 10^{-4}$ | 0.038 | 10 | 0.0003 | 10.62 | $5.54 \times 10^3$ | 12 | 0.917 | 0.149 | Charnock et al. (1994), Simpson (1993) |
| Chesapeake | $1.8 \times 10^4$ | $8.70 \times 10^{-5}$ | 0.033 | 10 | 0.0010 | 9.70 | $6.53 \times 10^3$ | 17 | 0.587 | 0.674 | Boicourt (1973) |
| Columbia | $2.2 \times 10^4$ | $1.05 \times 10^{-4}$ | 0.118 | 0 | 0.0036 | 6.32 | $8.21 \times 10^3$ | 30 | 0.214 | 4.675 | Hickey et al. (1998) |
| Gaspe | $6.0 \times 10^4$ | $1.08 \times 10^{-4}$ | 0.078 | 0 | 0.0120 | 12.88 | $9.27 \times 10^3$ | 111 | 0.116 | 8.634 | Mertz et al. (1988) |
| Soya | $7.0 \times 10^5$ | $1.02 \times 10^{-4}$ | 0.030 | 0 | 0.0028 | 68.99 | $1.41 \times 10^4$ | 39 | 1.747 | 0.572 | Ichiye (1991) |
| Tsugaru | $1.0 \times 10^6$ | $9.70 \times 10^{-5}$ | 0.030 | 0 | 0.0190 | 80.42 | $1.60 \times 10^4$ | 304 | 0.264 | 3.783 | Ichiye (1991) |
| Hudson | $1.0 \times 10^4$ | $9.30 \times 10^{-5}$ | 0.086 | 10 | 0.0013 | 4.66 | $6.79 \times 10^3$ | 19 | 0.247 | 1.895 | Bowden (1983) |

is very nearly 1 (Chapman and Lentz note that in all of their numerical experiments the value of the bracketed term did not deviate from 1 by more than 4%). Scaling the terms in Eq. (10) by the coastal current scale depth, width, and velocity given in Eqs. (3), (4), and (5), respectively, produces

$$y_b \sim \frac{f\rho_0}{\alpha g}\frac{\sqrt{g'h}(\sqrt{g'h}/f)}{\Delta\rho}. \tag{11}$$

Noting that $g' = (\Delta\rho/\rho_0)g$, this scaling reduces to the very simple form:

$$y_b \sim \frac{h}{\alpha}. \tag{12}$$

Finally, in nondimensional form, the bottom-slope parameter scaling is

$$\frac{R}{y_b} = \frac{\alpha R}{h}. \tag{13}$$

This parameter is a ratio between the scale width $R$ and the bottom-trapped width $y_b$. A value of the ratio larger than 1 indicates that the scale width is larger than the trapped width so that the coastal current experiences horizontal ''compression'' at its base. If the value of the ratio is smaller than 1, it indicates that the coastal current undergoes lateral expansion at its base beyond its scale width. Note, however, that the bottom slope parameter, $R/y_b$, is more than just a ratio of width scales. It is also a ratio between the bottom slope ($\alpha$) and the average isopycnal slope ($h/R$). Furthermore, it can be shown that the bottom slope parameter $R/y_b$ is equivalent to the slope Burger number defined as $N\alpha/f$ (Clarke and Brink 1985). Here, $N$ is the buoyancy frequency, $\alpha$ is the bottom slope, and $f$ is the Coriolis parameter.

The nondimensional parameter space ($h/H$, $R/y_b$) that comprises the ambient depth and bottom slope parameters is shown graphically in Fig. 3. The vertical axis is the ambient depth parameter [Eq. (6)]. Increasing values of $h/H$ reflect increasing coastal current–bottom interaction. The schematics in Fig. 4 depict the possibilities of the parameter space. Figure 4a illustrates the situation of $h/H < 1$, when buoyant water overlies a deep ambient ocean. This corresponds to the lower edge of the parameter space shown in Fig. 3 ($h/H \sim 0.1$). In comparison, Fig. 4b depicts the situation of $h/H > 1$, corresponding to the upper edge of the parameter space. In this instance, the estimated scale depth, $h$ is greater than the ocean depth, resulting in strong interaction between the bottom and the coastal current.

The horizontal axis of Fig. 3 is the bottom slope parameter [Eq. (13)]: increasing values of $R/y_b$ reflect increasing compression. Figure 4c is a schematic of the situation in which $R/y_b < 1$, for which the buoyant layer is expanded offshore to a width greater than its scale width $R$. This offshore expansion results in a weaker across-shore isopycnal gradient and, accordingly, a weaker across-shore baroclinic pressure gradient, $\partial P/\partial y$.

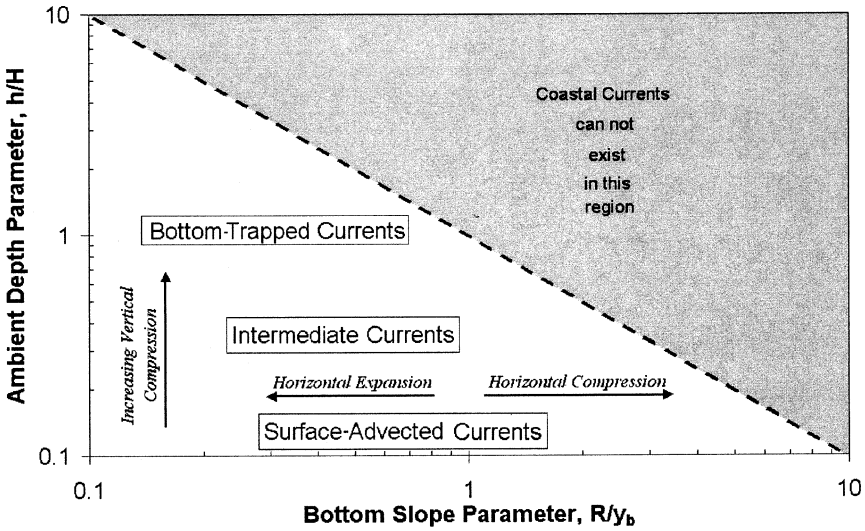


FIG. 3. A graph of the parameter space based upon the interaction parameters given in Eqs. (6) and (13). The vertical axis indicates the ambient depth parameter, $h/H$. The lower edge of the graph possesses small values of $h/H$ indicating that the coastal current is isolated from the bottom (surface-advected current), while the upper edge of the graph possesses large values of $h/H$ indicating that the coastal current is interacting with the bottom. The horizontal axis is the bottom slope parameter, $R/y_b$. Values on the left edge of the graph characterize coastal currents that are forced to grow wider than the buoyant scale ($R/y_b < 1$), while values on the right edge of the graph indicate that the current is compressed in width ($R/y_b > 1$). The sloping dashed line indicates the line given by $h/H = (R/y_b)^{-1}$, which arises for the singular geometrical configuration of a single linear bottom slope without a vertical coastal wall. Values below this line are possible, while values above it (in the gray region) are not.

The decreased pressure gradient in this situation causes the coastal current to form flatter isopycnal slopes. Through geostrophy this also corresponds to smaller values of alongshore velocities. In comparison, Fig. 4d depicts the situation in which $R/y_b > 1$, corresponding to the right-hand edge of the parameter space. In this instance, the bottom of the buoyant current is compressed closer to the shore than the scale width $R$. A consequence of the compression is to increase the pressure gradient $\partial P/\partial y$ and produce steeper isopycnal slopes.

It is important to note the limits of the nondimensional coastal current–shelf interaction space ($h/H$, $R/y_b$). The ambient depth parameter has obvious limits. As the value of $h/H$ tends to zero, the flow configuration approaches an infinitely deep ocean. This limit can be interpreted simply as a surface-advected coastal current. The other limit occurs as the value of $h/H$ tends to infinity. This limit is not physically realizable; as the water depth vanishes, the current scale grows very large compared to the scale depth, and the momentum balance will deviate from that of a geostrophic balance (what was a thin bottom frictional layer below a geostrophic layer becomes a thick frictional layer that occupies most or all of the water column). The primary force balance will differ; the pressure gradient and frictional drag balance and the scaling would no longer hold. The bottom slope parameter also has two limits. For small values of $R/y_b$, the bottom slope becomes increasingly flat. In this situation, the scaling predicts that the bottom-trapped distance $y_b$ will grow large. The other asymptote occurs when $R/y_b$ values are large. In such situations, the bottom slope can more appropriately be thought of as a coastal wall. Therefore, in this limit the coastal current evolves as a surface-advected current.

The bottom slope parameter $R/y_b$ is linked to the ambient depth parameter $h/H$, through the definition of $H$. For the special case of a bottom topography that can be described by a single bottom slope without a vertical wall, as shown in Figs. 2a and 2b, the definition of $H = \alpha R$ links the two parameters. For this situation, the only possible values in the parameter space fall on the line $h/H = (R/y_b)^{-1}$, which is shown as the sloping dashed line in Fig. 3. For more complex bottom topography, as shown in Figs. 2c and 2d, values are constrained to be below the line ($h/H < (R/y_b)^{-1}$). Thus, while it is possible to produce bottom-trapped coastal currents with small bottom slope parameter values ($h/H \sim 1$, $R/y_b < 1$), bottom-trapped coastal currents with large values of the bottom slope parameter space ($h/H \sim 1$, $R/y_b > 1$) are not realizable. The most horizontally compressed coastal currents possible (large values of $R/y_b$) are currents with $h/H$ values not much less than one (e.g., $h/H \sim 0.4$), described as ''intermediate'' currents in Yankovsky and Chapman (1997). For such a coastal current it is possible for the bottom slope parameter to be slightly greater than 1 ($R/y_b \sim 2$).

Oceanic coastal currents typically have temporally

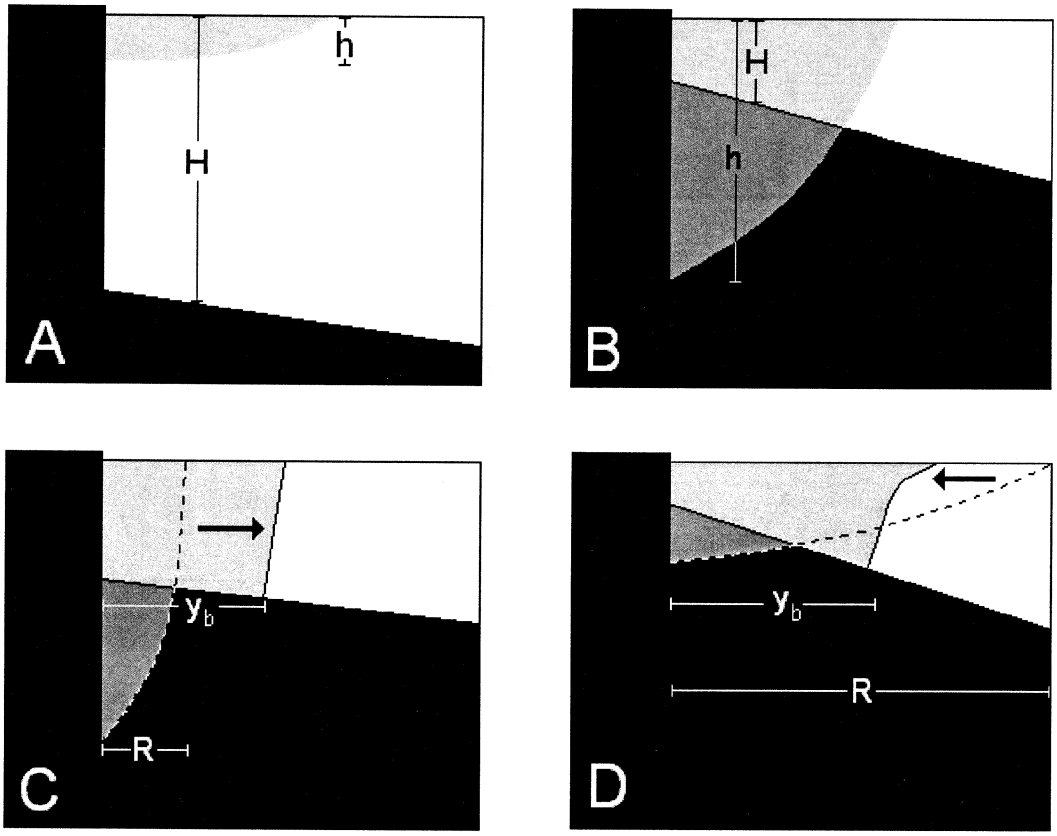


FIG. 4. Schematic depicting bottom depth, bottom slope parameter variations. Black indicates the (impermeable) solid of the coastline shore and bottom. The Margules front prediction of the frontal structure is shown in light gray. If the predicted frontal structure overlaps with bottom topography, this is depicted in dark gray. (a) A surface-advected current, in which $h/H < 1$. (b) The opposite: a bottom-trapped current in which $h/H > 1$. (c), (d) Bottom-trapped currents for which the bottom-trapped parameter has opposite effects: $R/y_b < 1$ in (c), indicating an expansion dominated current; $R/y_b > 1$ in (d), indicating a compression dominated current.

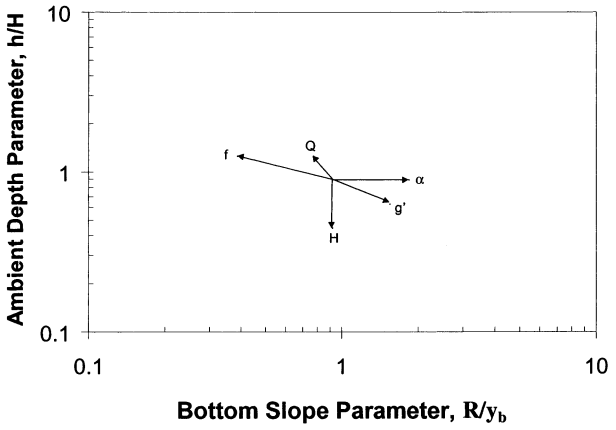


FIG. 5. Graph that illustrates the functional dependence of the parameter space based upon the three scale parameters and two topographic parameters. This graph was produced by taking a starting position near $h/H = 1$, $R/y_b = 1$ in the parameter space and doubling the value of each parameter individually (holding the others constant). Thus, each arrow indicates how, from the given starting point, a factor-of-2 increase in the value of the varied parameter would change the position of the coastal current in the parameter space.

variable source conditions due to seasonal and yearly variations. Outflow rates may vary by an order of magnitude or more, coupled with changes in the magnitude of the source density anomaly. Therefore, it is useful to explore how variations in the values of a coastal current's source characteristics can alter its location in the nondimensional parameter space ($h/H$, $R/y_b$). Figure 5 illustrates how a point in the parameter space, near $h/H = 1$, $R/y_b = 1$, changes with a factor-of-2 increase in $Q$, $f$, $g'$, $H$, or $\alpha$. From the initial point, five vectors originate. Each vector represents the shift in the parameter space for which each of the parameters was held constant except the varied parameter, which was doubled.

## 3. Experimental setup

The utility of the scaling analysis was examined through a program of laboratory experiments conducted at the Environmental Fluids Laboratory in the College of Marine Studies, University of Delaware. A rotating turntable 1.2 m in diameter was used for these exper-

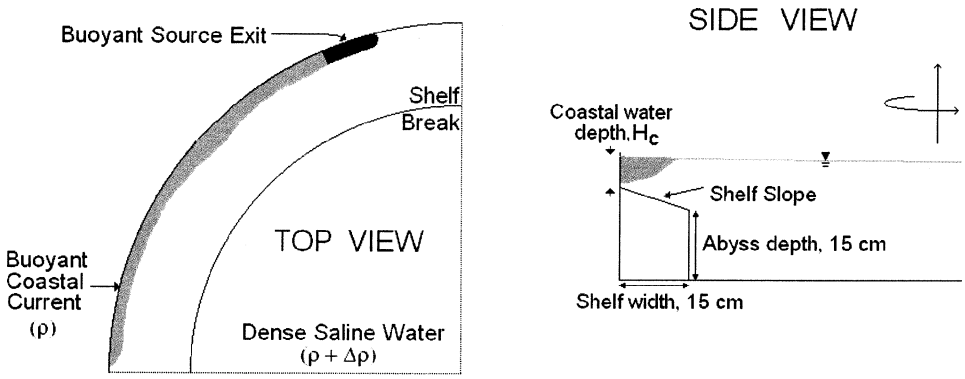


FIG. 6. Schematic depicting the experimental configuration using the sloping bottom tank. The tank is a cylinder (one quarter is shown above) with a radius of 60 cm. There is a ''continental shelf'' with a bottom slope of 1:3 extending offshore for 15 cm uniformly around the tank. Offshore of the continental shelf is a 15-cm abyss. The buoyant source is placed parallel to the coastline.

iments. It is constructed in such a manner that tanks of various configurations can be installed onto the turntable. For these experiments two tanks were used: a tank with a flat bottom ($\alpha = 0$) and a tank with a bottom slope of 1:3 ($\alpha = 0.333$). Figure 6 is a schematic portraying the experimental setup for the sloping bottom tank. The schematic is a quarter section of the actual turntable.

The tank is filled with ambient ocean water of a specified salinity, while freshwater is stored in a separate, corotating smaller reservoir, as a source for the buoyant outflow. The source for these experiments is a pipe, with a radius of 1 cm, set parallel to and in contact with the coast. Figure 6 shows the placement of the source in the experiments conducted. Experiments were terminated before the coastal current was allowed to propagate around the circumference of the entire tank; the longest experiments were allowed to run 320°, which corresponds to a distance of 335 cm. The turntable was set to a specified rotation rate before each experiment, and the ambient ocean fluid was allowed to reach solid body rotation before each experiment was begun. The table spins in a counterclockwise direction; thus, $f$ is positive.

Data in the experiments were collected by two means. From video records, velocities and geometrical information of the coastal current were measured with time. The buoyant outflow was marked using small concentrations of Rhodomine dye in order to facilitate flow visualization of the coastal current. The flow was seeded with hundreds of reflective surface drifters, typically 0.5 mm in size. These drifters were tracked in time and position using PIV (Particle Image Velocimetry) techniques, in order to provide information on the coastal current dimensions and velocities. Second, measurements were undertaken to determine the density field. Hypodermic probes of 0.8-mm diameter were located at specific points in the flow in order to obtain density cross sections of the selected coastal current. Fluid was sampled at these points and density was measured using an optical refractometer. Multiple experiments were conducted to construct an entire cross section of the density field.

Using such sampling methods, mean density transects in the offshore direction ($y$–$z$ plane) for three coastal currents were taken. The cross sections were taken at one downshelf location ($x = 50$ cm) by measuring density samples at various points in the $y$–$z$ plane. At each point density samples were taken to establish the mean density for the point. Six probes could be operated simultaneously during a single experiment; therefore, a number of experiments were undertaken to complete an entire cross section. Cross sections were constructed from the data of a number of horizontal transects. In some locations, overlapping vertical layers were added to establish vertical density gradients accurately. Variability existed in density measurements at a point within a single experiment: Variability at a point within multiple experiments was of the same magnitude. Density measurements were accurate to within 5% or better. Specific values of the parameters used in the experiments presented are tabulated in the next section.

Turntable accuracy is an important and difficult aspect of these experiments. The turntable is leveled to an accuracy of 0.0004 radians. The rotation rate is maintained at a specified rate, to within a $\Delta T = 0.01$ s. This corresponds, depending upon the rotation period of an experiment, to a relative rotation error of between 0.002 and 0.0001 rad $s^{-1}$. A Plexiglas cover is fitted over the turntable in order to eliminate surface wind stress and evaporative cooling. Water temperature was allowed to equilibrate to room temperature before experiments to minimize thermal differences.

## 4. Experimental results

This section will focus on the results of these experiments and compare them with the scaling analysis of coastal current–shelf interaction presented in section 2. Results are divided into three groups based upon the

TABLE 2. Laboratory experiments conducted. Values listed, in order, are coastal wall depth $H_c$; outflow rate $Q$; rotation period $T$; density anomaly $\Delta\rho$; Coriolis parameter $f$; reduced gravity anomaly $g'$; scale depth $h$; scale velocity $c$; scale width $R$; bottom slope $\alpha$; ambient ocean depth $H$; bottom depth parameter $h/H$; bottom-trapped length scale $y_b$; and bottom slope parameter $R/y_b$. Type indicates surface-advected (S), bottom-trapped (B), or intermediate (I).

| | Expt | | | | | | | |
|---|---|---|---|---|---|---|---|---|
| | A | B | C | D | E | F | G | H |
| $H_c$ (cm) | 7.00 | 10.50 | 7.00 | 10.00 | 10.00 | 2.50 | 1.25 | 0.50 |
| $Q$ (cm$^5$ s) | 1.33 | 5.84 | 10.01 | 6.67 | 6.67 | 6.67 | 7.00 | 10.01 |
| $T$ (s) | 35.00 | 6.00 | 14.00 | 6.00 | 14.00 | 10.00 | 6.00 | 15.00 |
| $\Delta\rho$ (g cm$^{-3}$) | 0.0025 | 0.0115 | 0.0255 | 0.0105 | 0.0050 | 0.0030 | 0.0105 | 0.0235 |
| $f$ (s$^{-1}$) | 0.36 | 2.09 | 0.90 | 2.09 | 0.90 | 1.26 | 2.09 | 0.84 |
| $g'$ (cm s$^{-2}$) | 2.45 | 11.21 | 24.68 | 10.24 | 4.89 | 2.94 | 10.24 | 22.76 |
| $h$ (cm) | 0.63 | 1.48 | 0.85 | 1.65 | 1.57 | 2.39 | 1.69 | 0.86 |
| $c$ (cm s$^{-1}$) | 1.24 | 4.07 | 4.59 | 4.11 | 2.77 | 2.65 | 4.16 | 4.42 |
| $R$ (cm) | 3.45 | 1.94 | 5.11 | 1.96 | 3.08 | 1.11 | 2.46 | 5.15 |
| $\alpha$ | 0.33 | 0.33 | 0.33 | 0.00 | 0.00 | 0.00 | 0.33 | 0.33 |
| $H$ (cm) | 8.15 | 11.15 | 8.70 | 10.00 | 10.00 | 2.50 | 2.07 | 2.22 |
| $h/H$ | 0.08 | 0.13 | 0.10 | 0.17 | 0.16 | 0.96 | 0.82 | 0.39 |
| $y_b = h/\alpha$ | 1.88 | 4.43 | 2.56 | $\infty$ | $\infty$ | $\infty$ | 5.08 | 2.57 |
| $R/y_b$ | 1.84 | 0.44 | 2.00 | 0.00 | 0.00 | 0.00 | 0.48 | 2.00 |
| Type | S | S | S | S | S | B | B | I |

value of the bottom depth parameter. Following the classification scheme of Yankovsky and Chapman (1997), these groups are designated as surface-advected, intermediate, and bottom-trapped coastal currents. Surface-advected currents are defined as experiments for which the value of the ambient depth parameter is less then 0.2 ($h/H < 0.2$). Bottom-trapped currents are defined as experiments in which the bottom depth parameter is $h/H > 0.8$. Intermediate currents lie between the range of surface-advected and bottom-trapped experiments, and should be marginally influenced by bottom bathymetry. Table 2 lists the experimental values of the parameters for all experiments presented in this paper. There are a total of eight experiments: five surface-advected (expts A–E), two bottom-trapped (expts F–G), and one intermediate case (expt H).

### *a. Surface-advected experiments*

Data for the surface-advected experiments ($h/H < 0.2$) should collapse with the coastal current scales ($R$, $h$, and $c$), and be independent of the value of the bottom slope parameter. Surface-advected experiments are designated A–E in Table 2. As tabulated, each experimental parameter has an ambient depth parameter of $h/H < 0.2$, while the bottom slope parameter values range from 0 to 2.0. Note that the five experiments used in this study to delineate the surface-advected current behavior arose from a large range of parameters, including both flat- and sloping-bottom tanks.

The dimensions of a coastal current were determined using flow visualization techniques described in section 3. The graphs of Fig. 7 show the evolution of the nose and width for the experiments listed in Table 2 as a function of time. Figure 7a is an $x$–$t$ plot of the nose (or leading edge of the current) position as a function of time for the five surface-advected experiments. Note that propagation velocities of the current are equal to the slope of the lines in the figure. Figure 7a is plotted in dimensional form: the ordinate is the downstream distance in centimeters, and the abscissa is the time in seconds. The results show a large spread in the $x$–$t$ plot among the five experiments. Directly beneath this graph is Fig. 7c, for which the data of Fig. 7a have been nondimensionalized by the coastal current scales. On the vertical axis, the downstream distance $x$ is scaled by the horizontal length scale $R$. For the abscissa, the experiment time $t$ is nondimensionalized by the rotation period $T$. The unit of the nondimensional quantity time/rotation period is analogous to days. The scaling collapses the $x$–$t$ data well.

Figure 7b is a plot of coastal current width data as a function of time for the five experiments listed in Table 2 as surface-advected experiments. Note that the coastal current width was not inferred from dye concentration, as dye concentrations can vary from experiment to experiment. Also, the use of dye concentrations to infer width is ambiguous because dye may occupy regions that are not dynamically active (e.g., dye may be advected or mixed to a region in which the velocities and pressure gradients are small). Rather, width information is determined from surface drifter records with the width being defined by the location of maximal shear. Width data are shown for up to 20 inertial periods; for subsequent times backward breaking instabilities are seen to form and the width of the coastal current becomes undefined. Beneath Fig. 7b are the same width data presented in nondimensional form as Fig. 7d. The data are seen to collapse approximately; the curves are similar in form, only differing by an offset on the $x$ axis. The horizontal offset between experiments arises from fact that each coastal current was measured at the same point ($x = 50$ cm) in the tank. When scaled, however, these correspond to different nondimensional distances downstream, and thus

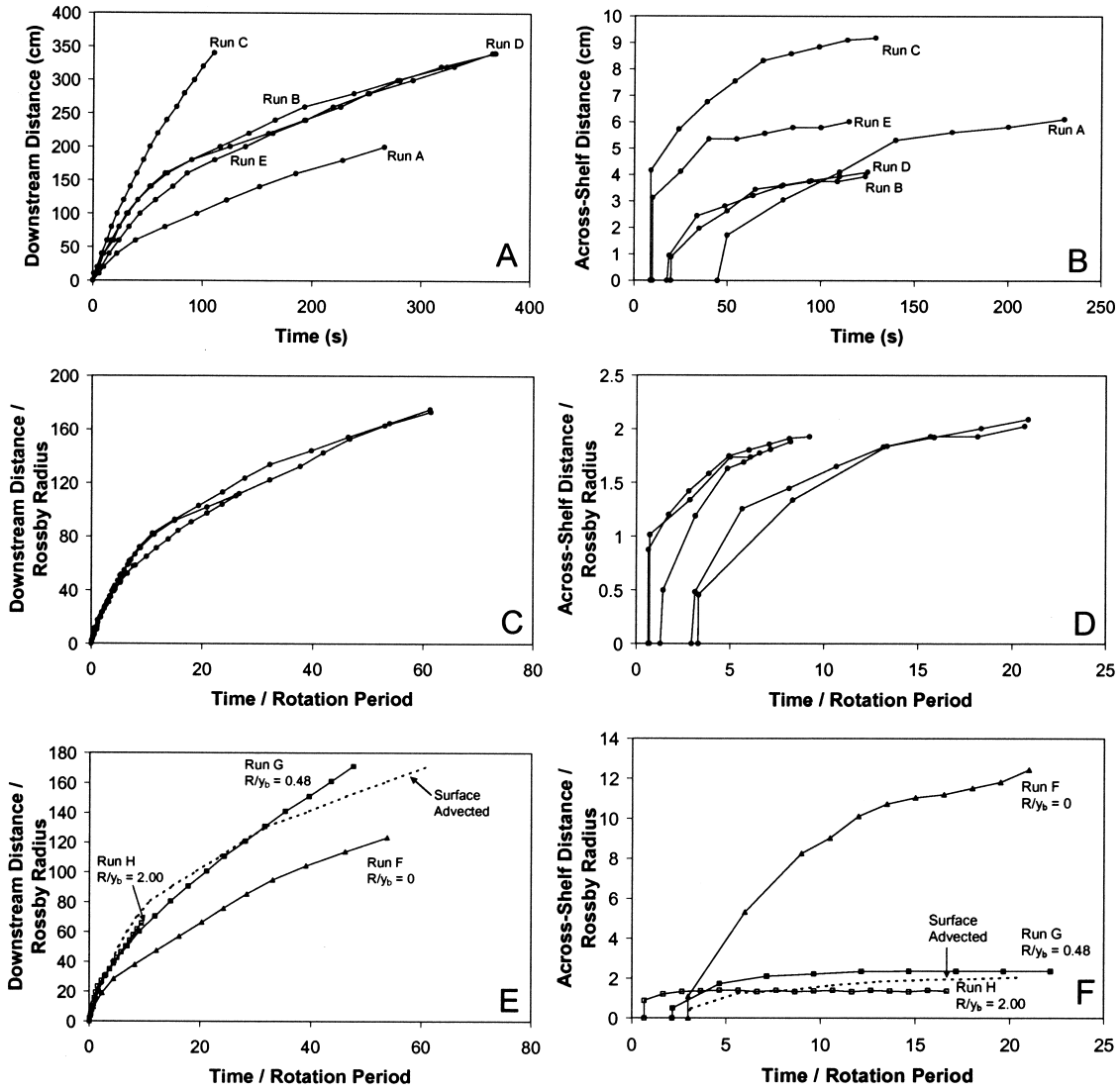


FIG. 7. Graphs of coastal current evolution. The left-hand panels display nose position (downstream distance from source) as a function of time. The right-hand panels display current width (at $x = 50$ cm) as a function of time. The upper two panels show data for surface-advected experiments (expts A–E from Table 2) plotted in dimensional form. The middle panels show the identical data for the same experiments plotted in nondimensional form. The lower panels show data for the bottom-trapped and intermediate experiments (expts F–H) plotted in nondimensional form. Also plotted in the lower panels is a curve representing the evolution of the surface-advected experiments for comparison.

the nose does not reach the measurement point at the same nondimensional time. Taking into account the horizontal offset the curves do, in fact, collapse well. To summarize, for surface-advected coastal currents the data collapse with the scales $R$ and $T$.

### *b. Bottom-trapped/intermediate experiments*

Table 2 also tabulates the values of parameters for three other experiments: two of which are bottom-trapped currents (experiments F, G; $h/H > 0.8$) and one of which is the intermediate case (experiment H; $h/H \sim 0.4$). These currents are analyzed to discriminate the role of the bottom slope parameter. As these experiments feel the influence of the bottom, large variations in their evolutions may be expected. Figure 7e is the nondimensional $x$–$t$ plot for these experiments. Also plotted is an averaged curve for the surface-advected data for comparison. The data do not collapse: Rather, there is a dependence of nose propagation upon the value of the bottom slope parameter; experiments with smaller values of bottom slope parameter have slower propagation.

The values of the bottom slope parameter for experiments G ($R/y_b = 0.48$) and H ($R/y_b = 2.0$) are perturbations about $R/y_b = 1$. In contrast, experiment F has the limiting value of a bottom slope parameter equal to zero. The downstream evolution of experiment F is significantly smaller than that of G and H in the across-

shelf direction. In comparison, the differences in downstream evolution in Fig. 7e between experiments G and H are small. The slopes of Fig. 7e suggests that the two experiments, G and H, have different final velocities: Experiment G moves downstream at a velocity approximately 50% slower than H. The final slope of experiment G is $\sim 0.23c$, while that of experiment H is $\sim 0.35c$.

The nose velocities of these coastal currents appear to reach a constant velocity as the slope of the $x$–$t$ plot becomes linear eventually ($t/T \sim 20$ days for experiment G; $t/T \sim 2.5$ days for experiment H). It will be shown later that these times correspond to the time when the coastal current width ceases to grow offshore. Taken together, this suggests that these trends are consistent with a coastal current encountering its offshore trapping limit. This effect can be seen in Fig. 7e, in which the evolution of the surface-advected coastal currents possesses larger values of downstream distance initially but smaller values subsequently. This supports the hypothesis that the offshore volume flux forced by the bottom Ekman layer slows the bottom-trapped coastal currents for small times. However, once the coastal current's offshore growth is arrested at its final trapped width, the nose velocity stays nearly constant. For the limiting case of flat bottom bathymetry of the coastal current of experiment F, the offshore-trapped width is located at infinity. Thus, the coastal current continues to grow offshore at all times; it is for this reason that its downstream propagation is significantly smaller relative to the coastal current of experiments G and H.

Figure 7f is a plot of the nondimensional across-shore width of the bottom-trapped currents. In the case of experiment F ($R/y_b = 0$), the coastal current width grows offshore continuously. The data show that the width grows offshore very quickly in comparison with the other experiments, reaching a distance of over $12R$ in width by the end of the experiment ($\sim$20 days). Also plotted are data for coastal currents G and H, as well as a representative offshore width curve for the surface-advected current. The coastal current of experiment G expands offshore more quickly than the surface-advected case and reaches an eventual offshore trapped width of about $2.2R$. In comparison, the coastal current of experiment H is constrained to a width narrower than the surface-advected case. This is consistent with the horizontal expansion of coastal currents for $R/y_b < 1$, and horizontal compression of coastal currents for $R/y_b > 1$ (see Fig. 3). Note that the coastal currents of experiments G and H reach their final offshore trapped widths quickly in comparison with the continually growing surface-advected experiment: Coastal current G reaches a maximum offshore extent at approximately 15 days, and experiment H reaches its maximum offshore extent at approximately 4 days. These times coincide with the locations in Fig. 7 at which the respective coastal current nose velocity reach a constant value.

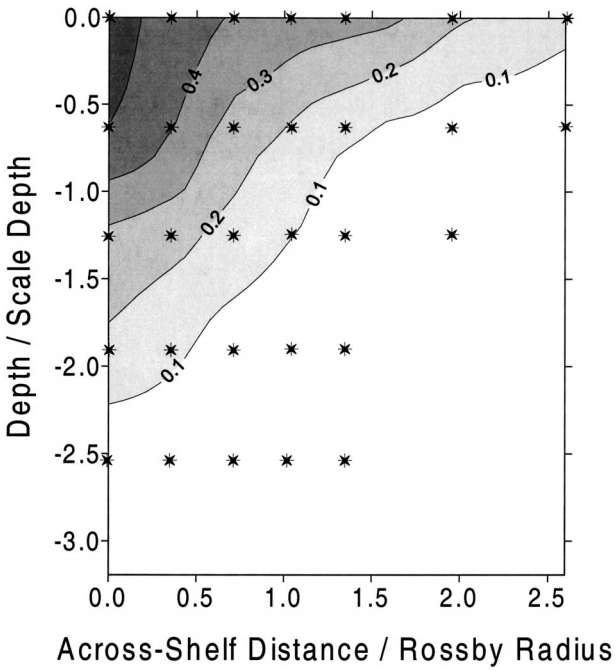


FIG. 8. Nondimensional plot of a mean density cross section through a surface-advected coastal current. The parameters that were used to make this plot are labeled expt E (see Table 1). The horizontal axis is across-shore distance normalized by the scale width $R$. The vertical axis is the depth normalized by the scale depth $h$. The contour values are the measured density anomaly normalized by the freshwater source density anomaly. The stars indicate points at which data were taken. For conciseness, data are only displayed to values of $z/h \sim 3$, whereas the bottom of the ocean is located at a value of approximately $-6.3z/h$. Note that the approximate slope of the isopycnals is 1 $h/R$.

### c. Density transects

Figure 8 is a graph of a nondimensional density cross section for the surface-advected current labeled experiment E in Table 2. The coastal floor is located at a value of $h/H = -6.3$, which is located below the region shown in the plot. The abscissa is nondimensional offshore distance ($y/R$), while the ordinate is nondimensional depth ($z/h$). The measured density anomaly is nondimensionalized by the density anomaly at the source ($\Delta\rho/\Delta\rho_0$). The star symbols on the plot indicate the locations at which data of mean density were taken. The largest density anomaly occurs on the surface against the coastal wall, as may be expected. The cross section of Fig. 8 shows that the buoyant coastal current occupies approximately $2$–$2.5R$ in width and $2$–$2.5h$ in depth. Note that the scale depth divided by the scale width ($h/R$) is a prediction of the average isopycnal slope; the data of the isopycnal slope are in agreement with the scale slope of 1 $h/R$. Note that the current has mixed with ambient ocean water by this distance, as demonstrated by the fact that the maximum density anomaly is about 0.55 at this downshelf location (The coordinates of the measurement location are $x/R \sim 16$,

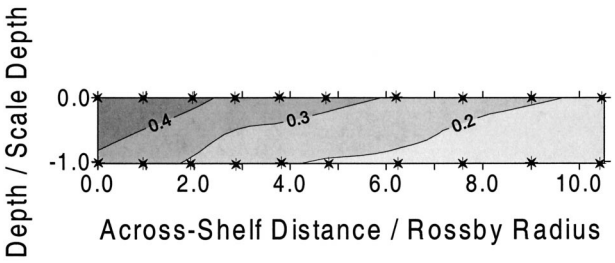


FIG. 9. Nondimensional plot of a mean density cross section through a bottom-trapped coastal current. The parameters that were used to make this plot are labeled expt F (see Table 1). The horizontal axis is across-shore distance normalized by the scale width *R*. The vertical axis is the depth normalized by the scale depth *h*. The contour values are the measured density anomaly normalized by the freshwater source density anomaly. The stars indicate points at which data were taken. The bottom of this graph is coincident with the ocean bottom. Note that the approximate slope of the isopycnals is 0.25*h*/*R*.

$t/T \sim 20$.) The density profile shows that the coastal current is not a two-layer configuration. Rather, there is a continuous variation of density and density gradients.

Figure 9 is a density transect, for the bottom-trapped experiment labeled experiment F in Table 2. The coastal floor is located at $h/H = -1.0$; thus the bottom of the plot indicates the location of the seabed. For this experiment, the coastal current has a bottom slope parameter value of zero. For this value, the offshore expansion of the coastal current should be rapid. This was previously seen in the coastal current width data plotted in Fig. 7f. Figure 9 reinforces this point clearly. The density anomaly shown for this transect extends over 10*R* offshore and possesses a maximum density anomaly of approximately 0.45 at the coast; density anomalies decrease to 0.2 at 10*R*. In comparison, Fig. 8 showed a range of density anomaly difference that varied from 0.5 to 0.1, and occurred in less than 1/5 of the nondimensional offshore distance. The nondimensional baroclinic pressure gradient of Fig. 9 is much less than that of the surface-advected current in Fig. 8. Interaction with the bottom has also affected the isopycnal slope of the buoyant layer: the isopycnal slopes are flatter in Fig. 9 in comparison to those of Fig. 8. The isopycnal slope in Fig. 9 is one-quarter as steep as that in Fig. 8, with a value of $\sim 1/4h/R$. In summary, the effect of the bottom slope in this case ($R/y_b \ll 1$) is to spread the density anomaly offshore and to flatten the isopycnal slopes, in addition to reducing the density gradient: because of geostrophy, the flattened isopycnals and small density gradient are consistent with the relatively smaller magnitudes of downshelf distances and velocities of this coastal current (see Fig. 7).

Figure 10 is a density transect taken from the intermediate coastal current labeled H in Table 2. The coastal floor is shown by the dark area extending from the coastal wall. As outlined in section 2, this experiment examines the point on the parameter space at which a coastal current can be most ''compression dominated''

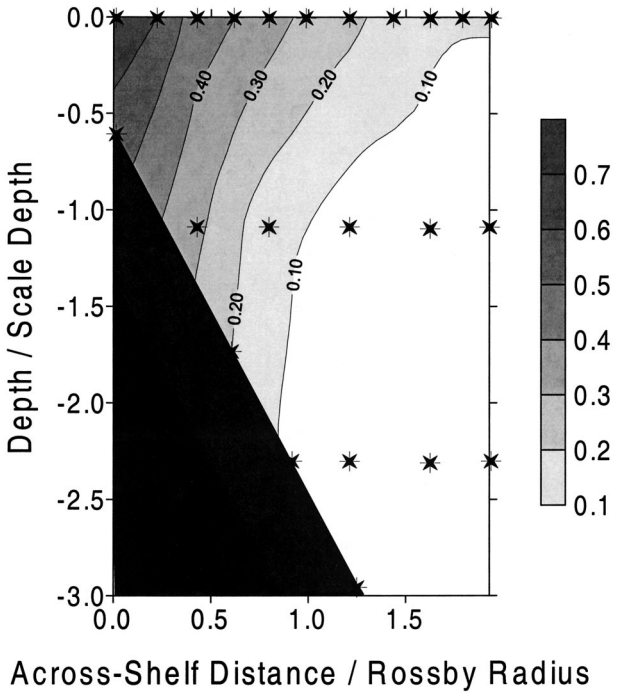


FIG. 10. Nondimensional plot of a mean density cross section through an intermediate coastal current. The parameters that were used to make this plot are labeled expt H (see Table 1). The horizontal axis is across-shore distance normalized by the scale width *R*. The vertical axis is the depth normalized by the scale depth *h*. The contour values are the measured density anomaly normalized by the freshwater source density anomaly. The stars indicate points at which data was taken. The dark gray area indicates the ocean bottom. Note that the approximate slope of the isopycnals is 2*h*/*R*.

($R/y_b \sim 2$) and yet still be influenced by the bottom as an intermediate coastal current ($h/H \sim 0.4$). The coastal current of experiment H is characterized by larger downshelf velocities and a narrower across-shore width in comparison with the surface-advected case of Fig. 8: The surface-advected transect (Fig. 8) possesses a current width of about 2–2.5*R*, while the experiment H (Fig. 10) shows a current width of only 1.5*R*. These numbers are consistent with the visually measured current widths shown in Fig. 7f of 2*R* and 1.5*R*, respectively. The maximum density anomaly for experiment H is higher than that for the surface-advected experiment (0.7 vs 0.5), and the across-shore width is less. This results in a larger across-shore density gradient, consistent with higher velocities in the coastal current. As in experiment F, the bottom interaction has also affected the isopycnal slope. As this experiment falls in the lateral compression region of the bottom slope parameter, $R/y_b > 1$, the isopycnal slope is steepened rather than flattened: for experiment H (Fig. 10), the isopycnal slope is increased to 2*h*/*R* from the scale slope of 1 *h*/*R*.

## 5. Comparison with oceanic observations

Classification of the characteristics of oceanic coastal currents is the ultimate purpose for this study. Available

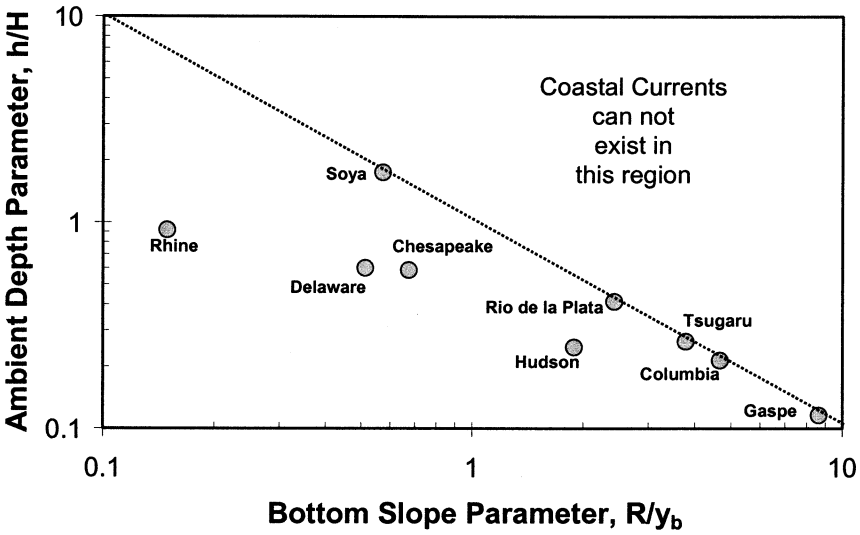


FIG. 11. Available oceanic coastal current data plotted in the two-parameter nondimensional space ($h/H$, $R/y_b$). The values attributed to the oceanic coastal currents used to produce this graph are in Table 1. Values are representative of typical outflow conditions for each of the buoyant outflows and are referenced in the table.

data for oceanic buoyant outflows that have been observed to form coastal currents are tabulated in Table 1. Using the coastal current parameters, $Q$, $f$, and $g'$ at the mouth of the outflow, and the coastal topography, the available data for the oceanic coastal currents are plotted as coordinates in the nondimensional parameter space ($h/H$, $R/y_b$) in Fig. 11.

A factor that must be considered in selecting values for $Q$ and $g'$ to characterize an outflow is where should those values be chosen. If a river empties into a large estuary, in which tidal mixing occurs, the values of $Q$ and $g'$ for the river discharge are not appropriate. The relevant values are the flow rate and the reduced gravity at the exit of the estuary, which subsequently forms a coastal current. Therefore values of Table 1 are computed based on $Q$, $g'$ values typical of the outflow exiting the mouth of the estuary.

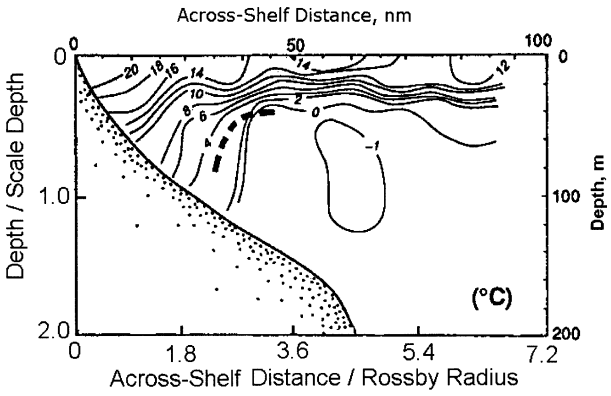


FIG. 12. Isotherm cross-section taken through the Soya Current adapted from Ichiye (1991). The transect was taken in Aug 1984. The nondimensional abscissa and ordinate were added onto the original figure. The values for $R$ and $h$ were computed based upon $Q$, $f$, and $g'$ estimates given in Ichiye (1991). The dashed line is the theoretical prediction of Ichiye (1991) based on conservation of potential vorticity within the buoyant layer. The Soya is a bottom-trapped coastal current.

Nine buoyant outflow sources are tabulated in Table 1: seven river systems (Chesapeake, Columbia, Delaware, Gaspe, Hudson, Rhine, and Rio de la Plata) and two strait outflows (Soya and Tsugaru). Four of the river systems have been characterized by a nonzero coastal wall depth, $H_c$. In each of these cases, this coastal wall depth has been estimated at 10 m. Examination of the bathymetry of the U.S. East Coast coastal currents (Hudson, Delaware, and Chesapeake) shows that there is an initial slope of $\sim$0.01 extending offshore for approximately a kilometer. Beyond this, the bottom slope becomes gentler by an order of magnitude. For the Rhine the initial slope of $\sim$0.01 extends 1 km offshore, and subsequently merges to the relatively flat North Sea slope of $\sim$0.0004. For the data of oceanic currents, there is a general trend from the top left to the bottom right in the nondimensional parameter space in Fig. 11. Note that the influence of the coastal wall, $H_c$, is more pronounced to the left hand of the parameter space (i.e., small values of the bottom slope parameter, $R/y_b$). The shallower the bottom slope (and/or the smaller the outflow is), the more pronounced is the effect of a coastal wall. This study concerns the dynamics of coastal currents in the absence of winds; therefore, it should be noted that the effects of strong upwelling or downwelling winds may affect the evolution of a coastal current (e.g., Fong and Geyer 2001).

Comparison with oceanic measurements of the temperature and density fields of coastal currents is useful. Ichiye (1991) describes observations of buoyant out-

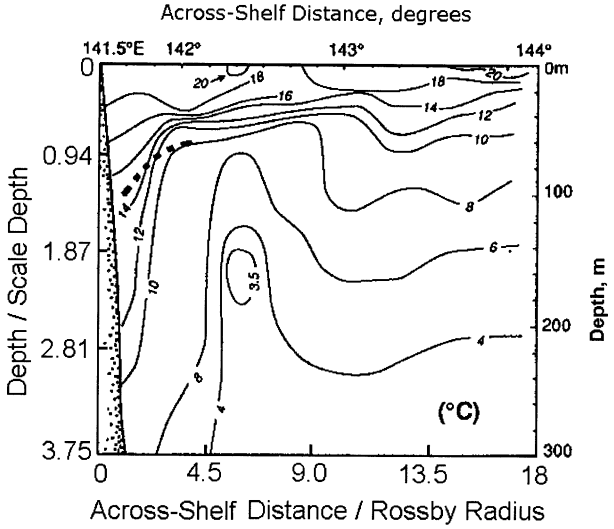


FIG. 13. Isotherm cross section taken through the Tsugaru Current adapted from Ichiye (1991). The transect was taken in Aug 1984. The nondimensional abscissa and ordinate were added onto the original figure. The values for $R$ and $h$ were computed based upon $Q$, $f$, and $g'$ estimates given in Ichiye (1991). The dashed line is the theoretical prediction of Ichiye (1991) based on conservation of potential vorticity within the buoyant layer. The Tsugaru is a surface-advected coastal current.

flows through Japanese straits. Figure 12 is a transect of temperature through the Soya current adapted from Ichiye (1991). From values of the coastal current parameters ($Q$, $f$, $g'$) tabulated by Ichiye, the coastal-current scale variables can be calculated ($h = 98$ m, $R = 17$ km). These values were used to nondimensionalize the ordinate and the abscissa in Figure 12. The bottom slope, $\alpha = 0.0028$, was estimated from the cross section. The bottom depth parameter, $H = 39$ m, was taken as the depth at one Rossby radius offshore. Therefore, the coastal current of Fig. 12 has an ambient depth parameter, $h/H = 1.64$, and a bottom slope parameter, $R/y_b = 0.57$. Thus, an appropriate classification for the Soya current is that it is a bottom-trapped coastal current. The structure seen in Fig. 12 is consistent with this classification (see schematic of Fig. 2b). The current width ($3R$) is slightly wider than a surface-advected coastal current (2–2.5$R$: see Figs. 8, 9). The average isothermal slope for distances up to $3R$ is about 1 $h/R$. Beyond $3R$, the flat isothermal slopes are likely to be associated with the temperature profiles of the ambient waters: they are not part of the dynamic coastal current.

Figure 13 is a transect also adapted from Ichiye (1991) taken through the Tsugaru current. Values of the coastal current scale parameters were calculated: (scale depth, $h = 80$ m, and Rossby radius, $R = 18$ km). These values were used to nondimensionalize Fig. 13. The water depth $H$ is approximately 300 m (taken at the depth one Rossby radius offshore). This depth is significantly greater than the scale depth. This coastal current can thus be classified as marginally surface advected with an $h/H$ value of 0.27, and thus is affected by some bottom interaction (to a distance of about 0.5$R$ offshore) but the majority of the coastal current is not. Notice the similarity (of the slopes and dimensions) between the surface-advected coastal currents in Fig. 8 (experimental expt E) and Fig. 13 (the Tsugaru transect). Both transects portray coastal currents that are approximately 2–2.5$R$ in width and 2–2.5$h$ in depth. They have nearly identical isopycnal/isothermal slopes ($\sim 1$ $R/h$). As before, the temperature contours beyond 2.5$R$ are not part of the dynamics of the coastal current.

Figure 14 comprises two density transects of the Delaware coastal current adapted from Münchow and Garvine (1993a,b). Values for the subtidal outflow and density anomaly through the mouth of the Delaware bay yields current scales of $h = 8.6$ m and $R = 6.4$ km during high discharge periods in the spring. These val-

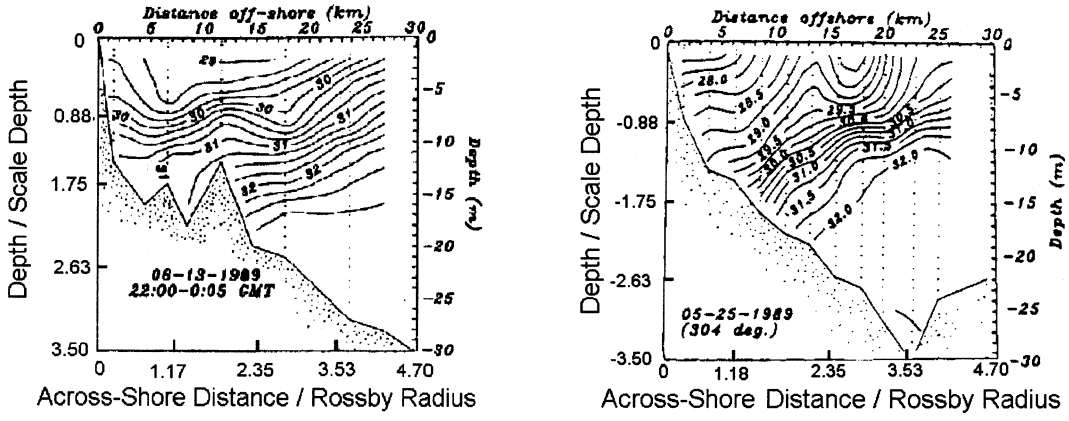


FIG. 14. Isopycnal transects taken of the Delaware coastal current. The left panel is adapted from Münchow and Garvine (1993b). This transect was taken in June 1989 during a period of light (4 m s$^{-1}$) downwelling winds. The right panel is adapted from Münchow and Garvine (1993a). This transect was taken in May 1989 during a period of weak variable winds. The plots have been modified from the original papers to include nondimensional axes. The values of $R$ and $h$ were derived using estimates for $Q$, $g'$, and $f$ taken from these papers.

ues are used to nondimensionalize Fig. 14. The ambient depth parameter, $h/H = 0.72$, and the bottom slope parameter, $R/y_b = 0.51$, are calculated based on these coastal current scales. This coastal current is classified as a weakly bottom trapped coastal current undergoing lateral expansion. The cross sections of Fig. 14 are consistent with this prediction; in both panels the Delaware coastal current is attached to the bottom as far offshore as $2.5R$. At the surface, the current has a width of approximately 4–5$R$ (defined at the point where a large number of isopycnals intersect the surface). The average isopycnal slope of this transect is $0.7h/R$, a value slightly less than that of the Soya Current. These transects were chosen in order to minimize the effect of wind on the plume, winds were mild prior to the observations. Generally, the winds were from the south, thus producing light upwelling conditions, which is likely to augment the across-shore width.

## 6. Summary

The objective of this paper is to examine the influence of shelf geometry upon the dynamics of coastal currents. A simple scaling is developed utilizing the bottom boundary layer trapping mechanism of Chapman and Lentz (1994). The scaling is based upon flow variables ($Q$, $g'$, $f$) of the coastal current and variables describing the shelf geometry ($h$, $\alpha$). A two-variable nondimensional parameter space ($h/H$, $R/y_b$) is proposed to classify the dynamics of coastal currents. The ambient depth parameter, $h/H$, reflects the fraction of the available depth occupied by the buoyant coastal current; the bottom slope parameter, $R/y_b$, the ratio of the internal Rossby radius to the bottom-trapped width, describes the effect of the slope on the dynamics of the coastal current. The resulting parameter space delineates surface-advected currents, which do not depend upon the bottom slope parameter, and bottom-trapped currents, which do. It is shown that for small values of the bottom slope parameter (due to, for instance, a relatively flat bottom) the coastal current will undergo lateral expansion that will result in a wider, slower flow. Coastal currents can only inhabit the parameter space in the region defined by $h/H \leq (R/y_b)^{-1}$. Thus, a limited area exists in the nondimensional parameter space in which the bottom slope parameter can be larger than 1 and the ambient depth parameter approximately unity; such coastal currents experience lateral compression and tend to be faster and narrower than a surface-advected plume.

Laboratory experiments were undertaken in order to test the proposed scaling. Flow visualization of the laboratory coastal currents were utilized to determine the evolution of the coastal current. Growth rates of both across-shelf width and downshelf length were determined. Additionally, density cross sections of the coastal current were resolved. The data are shown to agree with the classification of the coastal currents of the nondimensional parameter space. Currents with small values of the bottom slope parameter flow downstream slowly and are wider in extent than similar surface-advected currents: density cross sections confirm that the baroclinic pressure gradient in such coastal currents is weaker than that of surface-advected currents. Available observations of oceanic coastal currents were examined: the data show that these observations are in accord with the proposed nondimensional scaling.

*Acknowledgments.* Discussions with Rich Garvine and Kuo Wong throughout the course of our research were inspiring. We also thank Mike Whitney for constant critical discussions and valuable critiques. We are grateful to Dean Thoroughgood for fostering the creative environment of the POSE program in the College of Marine Studies and the Okie Fellowship for financial support. Thanks are due to Andreas Münchow for collegial support in sharing data regarding the Rio de la Plata outflow.

## REFERENCES

Blanton, J. O., and L. P. Atkinson, 1983: Transport and fate of river discharge on the continental shelf of the southeastern United States. *J. Geophys. Res.,* **88** (C8), 4730–4738.

Boicourt, W. C., 1973: The circulation on the continental shelf from Chesapeake Bay to Cape Hatteras. Ph.D. thesis, The Johns Hopkins University, 183 pp.

Bowden, K. F., 1983: *Physical Oceanography of Coastal Waters.* Halsted Press, 302 pp.

Bracalari, M., E. Salusti, S. Sparnocchia, and E. Zambianchi, 1989: On the role of the Froude number in geostrophic coastal currents around Italy. *Oceanol. Acta,* **12,** 161–166.

Chao, S. Y., 1988: River-forced estuarine plumes. *J. Phys. Oceanogr.,* **18,** 72–88.

Chapman, D. C., and S. J. Lentz, 1994: Trapping of a coastal density front by the bottom boundary layer. *J. Phys. Oceanogr.,* **24,** 1464–1479.

Charnock, H., K. R. Dyer, J. M. Huthnance, P. S. Liss, J. H. Simpson, and P. B. Tett, 1994: *Understanding the North Sea System.* Kluwer, 222 pp.

Clarke, A. J., and K. H. Brink, 1985: The response of stratified, frictional flow of shelf and slope waters to fluctuating large-scale, low-frequency wind forcing. *J. Phys. Oceanogr.,* **15,** 439–453.

D'Hieres, G. C., H. Didelle, and D. O. Baton, 1991: A laboratory study of surface boundary currents: Application to the Algerian Current. *J. Geophys. Res.,* **96** (C7), 12 539–12 548.

Fong, D. A., 1998: Dynamics of freshwater plumes: Observations and numerical modeling of the wind-forced response and alongshore freshwater transport. Ph.D. dissertation, MIT/WHOI, 172 pp.

——, and W. R. Geyer, 2001: Response of a river plume during an upwelling favorable event. *J. Geophys. Res.,* **106** (C1), 1067–1084.

Garvine, R. W., 1974: Physical features of the Connecticut River outflow during high discharge. *J. Geophys. Res.,* **79,** 831–846.

——, 1977: Observations of the motion field of the Connecticut River plume. *J. Geophys. Res.,* **82,** 441–454.

——, 1995: A dynamical system for classifying buoyant coastal discharges. *Cont. Shelf Res.,* **15** (13), 1585–1596.

——, and J. D. Monk, 1974: Frontal structure of a river plume. *J. Geophys. Res.,* **79,** 2251–2259.

Hickey, B. M., L. J. Pietrafesa, D. A. Jay, and W. C. Boicourt, 1998: The Columbia River plume study: Subtidal variability in the

velocity and salinity fields. *J. Geophys. Res.,* **103** (C5), 10 339–10 368.
Ichiye, T., 1984: Some problems of circulation and hydrography of the Japan Sea and the Tsushima Current. *Ocean Hydrodynamics of the Japan and East China Seas,* Elsevier, 15–54.
——, 1991: Outflows from straits. *Oceanography of Asian Marginal Seas,* K. Takano, Ed., Elsevier, 223–230.
Lentz, S. J., and K. R. Helfrich, 2002: Buoyant gravity currents along a sloping bottom in a rotating fluid. *J. Fluid Mech.,* in press.
Mertz, G., M. I. El-Sabh, and D. Proulx, 1988: Instability of a buoyancy-driven coastal jet: The Gaspe Current and its St. Lawrence precursor. *J. Geophys. Res.,* **93** (C6), 6885–6893.
Münchow, A., and R. W. Garvine, 1993a: Buoyancy and wind forcing of a coastal current. *J. Mar. Res.,* **51,** 293–322.
——, and ——, 1993b: Dynamical properties of a buoyancy-driven coastal current. *J. Geophys. Res.,* **98** (C11), 20 063–20 077.
Nof, D., and T. Pichevin, 2001: The ballooning of outflows. *J. Phys. Oceanogr.,* **31,** 3045–3058.
Park, K., 1966: Columbia River plume identification by specific alkalinity. *Limnol. Oceanogr.,* **11,** 118–120.
Pichevin, T., and D. Nof, 1997: The momentum imbalance paradox. *Tellus,* **49A,** 298–319.
Rennie, S. E., J. L. Largier, and S. J. Lentz, 1999: Observations of a pulsed buoyancy current downstream of Chesapeake Bay. *J. Geophys. Res.,* **104** (C8), 18 227–18 240.
Sanders, T. M., and R. W. Garvine, 1996: Frontal observations of the Delaware coastal current source region. *Cont. Shelf Res.,* **16,** 1009–1021.
Simpson, J. H., W. G. Bos, F. Schirmer, A. J. Souza, T. P. Rippeth, S. E. Jones, and D. Hydes, 1993: Periodic stratification in the Rhine ROFI in the North Sea. *Oceanol. Acta,* **16,** 23–32.
Stefansson, U., and F. A. Richards, 1963: Processes contributing to nutrient distribution off the Columbia River and Strait of Juan de Fuca. *Limnol. Oceanogr.,* **8,** 394–410.
Stern, M. E., J. A. Whitehead, and B.-L. Hua, 1982: The intrusion of a density current along the coast of a rotating fluid. *J. Fluid Mech.,* **123,** 237–265.
Sugimoto, T., 1990: A review of recent physical investigations on the straits around the Japanese Islands. *The Physical Oceanography of Sea Straits,* L. J. Pratt, Ed., Kluwer, 191–209.
Whitehead, J. A., and D. C. Chapman, 1986: Laboratory observations of a gravity current on a sloping bottom: The generation of shelf waves. *J. Fluid Mech.,* **172,** 373–399.
Yankovsky, A. E., and D. C. Chapman, 1997: A simple theory for the fate of buoyant coastal discharges. *J. Phys. Oceanogr.,* **27,** 1386–1401.